PFG (2022) 90:391–411
https://doi.org/10.1007/s41064-022-00210-2

ORIGINAL ARTICLE

Remote Sensing Techniques for Bridge Deformation Monitoring at Millimetric Scale: Investigating the Potential of Satellite Radar Interferometry, Airborne Laser Scanning and Ground-Based Mobile Laser Scanning

Matthias Schlögl[1] · Peter Dorninger[2] · Maciej Kwapisz[3] · Marian Ralbovsky[3] · Roland Spielhofer[3]

Received: 11 February 2022 / Accepted: 8 June 2022 / Published online: 30 June 2022

Abstract

In light of ageing infrastructure, structural condition assessment is a key prerequisite for the provision of reliable, safe and performant infrastructure networks. However, full systematic condition inspections across large transport networks are extremely resource intensive. Thus, network-wide continuous structural monitoring is hardly feasible using classical engineering assessment methods. Modern remote sensing techniques open up new possibilities for infrastructure assessment and monitoring. Three different methods for rapid, contactless and non-invasive infrastructure deformation monitoring are evaluated: (1) satellite radar interferometry (InSAR), (2) airborne laser scanning (ALS) using unmanned aerial vehicles (UAV) and (3) vehicle-mounted mobile laser scanning (MLS). All methods are tested at an integral concrete bridge in Vienna, Austria, and results are contrasted to reference measurements available from several water-level gauges. In addition, thermal deformation is modelled based on the prevailing environmental conditions. Results show that all methods are well capable of detecting general deformation trends, albeit exhibiting different stages of maturity. While the main application of InSAR lies in long-term continuous deformation measurement of the overall structure, MLS and ALS have the benefit of providing a wealth of data through measurement campaigns. All three contactless measurement methods are suitable for supplementing current structural condition assessments.

Keywords Infrastructure monitoring · Structural health monitoring · Remote sensing · Sentinel-1 · Persistent scatterer · InSAR · Laser scanning · Mobile mapping · Thermal deformation modelling

Zusammenfassung

Fernerkundungstechniken für die Überwachung von Brückenverformungen im Millimeterbereich. Angesichts alternder Infrastruktur stellt die Zustandserfassung von Ingenieurtragwerken eine wichtige Voraussetzung für die Bereitstellung zuverlässiger, sicherer und leistungsfähiger Infrastrukturnetze dar. Vollständige systematische Inspektionen in großen Verkehrsnetzen sind jedoch äußerst ressourcenintensiv. Daher ist eine netzweite, kontinuierliche Bauwerksüberwachung mit klassischen Bewertungsmethoden kaum machbar. Moderne Fernerkundungstechniken eröffnen neue Möglichkeiten für die Bewertung und das Monitoring von Tragwerken. Drei verschiedene Methoden zum schnellen, berührungslosen und nicht-invasiven Deformationsmonitoring werden bewertet: (1) Satelliten-Radarinterferometrie (InSAR), (2) Airborne Laser

✉ Matthias Schlögl
matthias.schloegl@zamg.ac.at

[1] Department for Earth Observation and Geoinformation, Central Institute for Meteorology and Geodynamics, Hohe Warte 38, 1190 Vienna, Austria

[2] 4D-IT GmbH, Emil Kögler-Gasse 13, 2511 Pfaffstätten, Austria

[3] Transportation Infrastructure Technologies, Austrian Institute of Technology, Giefinggasse 2, 1210 Vienna, Austria

Scanning (ALS) mit unbemannten Luftfahrzeugen (UAV) und (3) fahrzeuggestütztes mobiles Laserscanning (MLS). Alle Methoden werden an einer integralen Betonbrücke in Wien getestet, und mit Referenzmessungen eines Schlauchwaagensystems verglichen. Zusätzlich wird die thermische Verformung der Brücke unter Berücksichtigung der vorherrschenden Umweltbedingungen modelliert. Die Ergebnisse zeigen, dass alle Methoden trotz unterschiedlichen Genauigkeitspotentials gut in der Lage sind, allgemeine Verformungstrends zu erkennen. Während die Hauptanwendung von InSAR im langfristigen, kontinuierlichen Deformationsmonitoring der Gesamtstruktur liegt, haben MLS und ALS den Vorteil, im Rahmen von Messkampagnen umfassende Daten über den Zustand des Bauwerks bzw. der Fahrbahnoberfläche zu liefern. Alle drei Fernerkundungsmethoden eignen sich daher gut als Ergänzung der aktuellen Zustandsbewertung.

1 Introduction

Structural health monitoring of critical infrastructure is of major importance for ensuring the safety and smooth functioning of societies. Among various types of infrastructures, bridges stand out as assets of particular interest due to their widespread usage, their importance as key elements of infrastructure networks as well as their exposure to potentially heavy load and adverse environmental conditions. Recent tragic examples of bridge failures such as the Mexico City Metro overpass collapse (Mexico, 2021), the collapses of *Nanfang'ao Bridge* (Taiwan, 2019), *Majerhat Bridge* (India, 2019) and *Ponte Morandi* highway bridge (Italy, 2018) have illustrated not only the prevalence of the problem, but also the potentially severe impacts of bridge failure, including loss of life and substantial economic damages. Consequently, the continuous assessment of structural safety, including the measurement of structural deformation, does play an essential role (Bao et al. 2019).

Naturally, bridges exhibit movements due to temperature changes, which are estimated when designing the structure (Roeder 2003; Moorty and Roeder 1992). Bridge deformations strongly depend on the bridge design as well as the materials used. In general, two patterns of bridge deformation prevail, which are caused by either diurnal or seasonal temperature variation. Daily displacements of typical statically determined bridges are usually less than 1 cm, albeit deformations of up to several centimeters can be expected for integral bridges (Arsoy 2008), and deformations can even exceed 25 cm for large suspension bridges (Zhou et al. 2020). In addition, seasonal and long-term displacements due to shrinkage and creep can be an order of magnitude higher (Praxmarer and Reiterer 2007).

Historically, structural health monitoring as well as the measurement of bridge deformation was conducted using a variety of different systems (Middleton et al. 2016; Seo et al. 2016). Geodetic measurements in course of detailed bridge inspections were among the first, measuring deformation mostly at midspans and above piers. In the case of continuous monitoring, permanent sensor installation is necessary, for example using water-level pressure gauges or linear variable differential transformer (LVDT) sensors. These technologies require a reference point that is considered as non-moving. With water-level gauge systems, it is usually the abutment, while LVDT sensor systems typically use a ground point below the bridge as reference (Geier et al. 2014).

In recent decades, new technologies enabled new ways of measuring bridge deformation. The operation of global navigation satellite systems (GNSS) opened up possibilities to measure position of selected points without any reference on Earth's surface with millimetric to centimetric accuracy (Wang et al. 2021). The GNSS technology is particularly useful for cable-stayed bridges with very long spans (Xi et al. 2018), where application of other methods is not feasible and deformations in order of 10 cm are expected.

The above-mentioned technologies deliver bridge deformation data at a few selected points that are considered as decisive. Further technology advancements enabled acquisition of the bridge shape not only at few selected points, but at the whole surface. Photogrammetric measurements can be used to track a grid of points on the bridge using camera systems. One application of a photogrammetry method for monitoring the displacement of reinforced concrete bridge columns was presented by Alemdar et al. (2011), who report a measurement accuracy of approximately 1 mm. Using LVDT-sensor systems for comparative purposes, the technique showed good performance under the tested conditions.

Terrestrial laser scanning (TLS) devices provide point cloud data, which can be used to reconstruct the bridge shape. The points deviate from the scanned surface usually in the mm to cm range, therefore fitting of curves or surfaces is a common step in post-processing (Ye et al. 2018). Apart from 3D-model creation, TLS does have a wide variety of applications in bridge asset management, including quality inspection, structural health monitoring and deformation monitoring (Rashidi et al. 2020; Mukupa et al. 2016). Mounting of laser scanning devices on mobile platforms (vehicles, UAVs) increases the system mobility at the cost of additional uncertainties regarding the positioning. Mobile mapping applications range from road edge extraction (McElhinney et al. 2010) via deformation monitoring of retaining structures (Kalenjuk et al. 2019) to as-built model generation of tunnels (Arastounia 2016).

Distributed optical fiber sensing systems measure strain in an optical fibre that is attached to the bridge (Casas and Cruz 2003). The ability to measure the strain along the whole fibre enables to calculate the shape of bridge deformation. This technology was also tested on concrete structures with cracks (Li et al. 2021).

The use of satellite-based synthetic aperture radar (SAR) data is a relatively new approach in infrastructure monitoring. While there have been some studies in the last decade describing the successful use of commercial high-resolution X-band SAR data for measuring bridge deformation (Lazecky et al. 2017), the applications remained limited due to data availability. Just recently, the free and worldwide availability of SAR data, which came along with launches of Sentinel-1A and Sentinel-1B in April 2014 and 2016, respectively, sparked new interest in infrastructure deformation monitoring using satellite-based SAR interferometry (Macchiarulo et al. 2022; Schlögl et al. 2021). The single look complex (SLC) products delivered by the Sentinel-1 pair of satellites provide C-band SAR data (centre frequency: 5.405 GHz) at comparatively high resolution. Sentinel-1 SLC data feature a pixel spacing of 2.3 m (range) times 14.1 m (azimuth) and are available at a high temporal resolution of 6 days per orbit. Due to their sun-synchronous orbits, revisit times decrease and overlapping swaths increase towards both poles. In addition, almost global coverage renders this method interesting for network-wide assessments at low cost. Current advances in the area of bridge monitoring using InSAR do include the integration of information on the structural mechanics of bridges into the displacement time series analysis workflow (Qin et al. 2021).

Although contactless measurement technologies provide the comfort of remote measurement and the advantage of area-wide coverage of the bridge's surface, generally a lower measurement accuracy is to be expected. While the strengths and weaknesses of many of these individual measurement techniques are comparatively well known, an actual juxtaposition of selected methods, including an assessment of their potential based on a quantitative analysis of resulting deformation patterns, is still outstanding. Consequently, the goal of this work is to contribute to development of non-destructive and contactless testing methods for structural condition assessment without the demand for marked reference points. Focus was put on rapid acquisition methods which should be able to measure many bridges in short time, so that whole road sections can be processed quickly without disturbing traffic. The requirements of rapid acquisition, remotely sensed measurement and data-based condition assessment led to the choice of three techniques for bridge deformation measurement, which are described, applied and contrasted in the following (c.f. Fig. 1): (a) satellite radar interferometry (InSAR), (b) airborne laser scanning (ALS) using unmanned aerial vehicles (UAV) and (c) mobile laser scanning (MLS) using a vehicle that measures the bridge while passing over it. The comparative assessment is illustrated at the example of an integral concrete bridge located in the Danube harbour of Vienna, Austria. Validation of results is performed using in situ measurements obtained from a water-level gauge, as well as modelled bridge deformation based on environmental conditions. All methods rely on the assessment of relative differences in a local environment.

2 Data and Methods

2.1 Study Area

An integral concrete bridge (i.e. a bridge without bearings and expansion joints in its superstructure) does serve as a study object in this comparative assessment of remote sensing methods. Stretching across the Danube Canal, the 'side harbor bridge' (German: *Seitenhafenbrücke*) is located in the port of Vienna at N48°10′37.2″/E16°27′50.4″. The bridge consists of two river bank structures with a span of 32 m each and a river structure with a span of 64.7 m, resulting in a total length of 128.7 m. Two lanes for motor traffic as well as a path for pedestrians and bicycles result in a width of 15 m. For details on structural engineering it is referred to Kral et al. (2012) and Geier et al. (2014).

The temporal coverage of the measurements depends on the measurement method used. InSAR data are available over the whole time period between January 2015 and

Fig. 1 Investigated remote sensing measurement methods: **A** InSAR (Sentinel-1; source: ESA/ATG medialab (2014)); **B** UAV-ALS (4DU-Scanner; source: 4D-IT); **C** MLS (RoadSTAR, source: AIT)

October 2020 quite consistently with measurements every 6 days per orbit. There are only single, minor data gaps, resulting in a sampling rate of twelve instead of 6 days on 3–5 occasions per orbit (c.f. Fig. 4). ALS and MLS measurements were conducted on 2020-04-09. To capture the full diurnal variations of the temperature-caused bridge deformations, measurements took place in the morning (low temperature) and early afternoon (highest daytime temperature) with both sensor systems. An additional measurement took place on 2020-10-21 with the ALS system.

Points with information on surface deformation as derived via InSAR cover the entire surface of the bridge. For ALS and MLS, the edge beam and the road surface of the bridge were monitored, both of which are usually directly attached to load-bearing bridge parts. A local reference system was defined based on a reference point in the stable northern area of the bridge (Fig. 2).

2.2 In Situ Measurement

Due to the unique bridge characteristics, a comprehensive monitoring system was installed during bridge construction (Geier et al. 2014). Among other sensors, the measurement setup includes electronic water-level gauges used for measuring vertical bridge deformation, laser distance sensors to capture bridge elongation and temperature sensors to obtain concrete temperature. The measurements are available for most of the time between December 2011 and June 2017, at which point the monitoring system was no longer actively maintained to provide quality-controlled data on an operational basis. To provide a ground truth for the remote sensing measurements, the system was reactivated to provide quality-controlled measurements between January and June 2020. The location of the in situ deformation sensors is shown in Fig. 3.

2.3 InSAR

The InSAR analysis is based on Sentinel-1 Single Look Complex (SLC) data products acquired in Interferometric Wide (IW) swath mode. These IW SLC products, which are generated by applying the TOPSAR (Terrain Observation with Progressive Scans SAR) technique (Zan and Guarnieri 2006), feature a total swath width of 250 km and comprise three sub-swaths, which again consist of several bursts. In order to facilitate the data processing, the images of the IW SLC products are available at a common pixel spacing grid with a resolution of 2.3 m by 14.1 m in range and azimuth, respectively (ESA 2021). The time period under investigation in this analysis covers four full years and ranges from October 2016 to October 2020 (Fig. 4). Data from both Sentinel-1A and Sentinel-1B have been taken into account, resulting in a temporal resolution of 6 days for each orbit (Table 1). Since Vienna is covered by four different orbits (Fig. 5), four IW SLC products are available within every 6 days.

The overall processing chain employed to obtain deformation time series of the study object comprises two major pipelines: (1) the InSAR pipeline, featuring single leader InSAR processing as well as the actual PSI analysis; and (2) the pipeline for statistical post-processing of the InSAR time series. The complete underlying framework is presented in detail in Schlögl et al. (2021), the core elements of the workflow are briefly summarised in the following.

The InSAR processing pipeline comprises the following steps:

- *Identification of relevant orbits* The Vienna metropolitan area is covered by two ascending (73, 146) and two descending (22, 124) orbits (Fig. 5).
- *Data acquisition* Approximately, 240 Sentinel-1 scenes were acquired for each of the four orbits for the time period October 2016 to October 2020 (Fig. 4, Table 1).
- *Pre-processing of Sentinel-1 SLC data* Single leader InSAR preprocessing of Sentinel-1 data (i.e. coregistration, leader and supporter scene selection, interferogram generation and stacking) was performed using SNAP, the 'Sentinel Application Platform' (Foumelis et al. 2018; Delgado Blasco and Foumelis 2018).

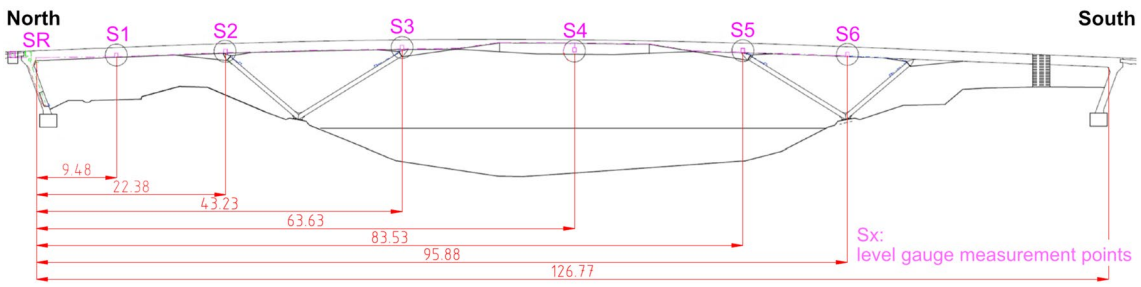

Fig. 2 Reference system of study area. The local reference point is located at the north abutment of the bridge at SR. SR and S[1-6] denote the water-level gauge measurement locations

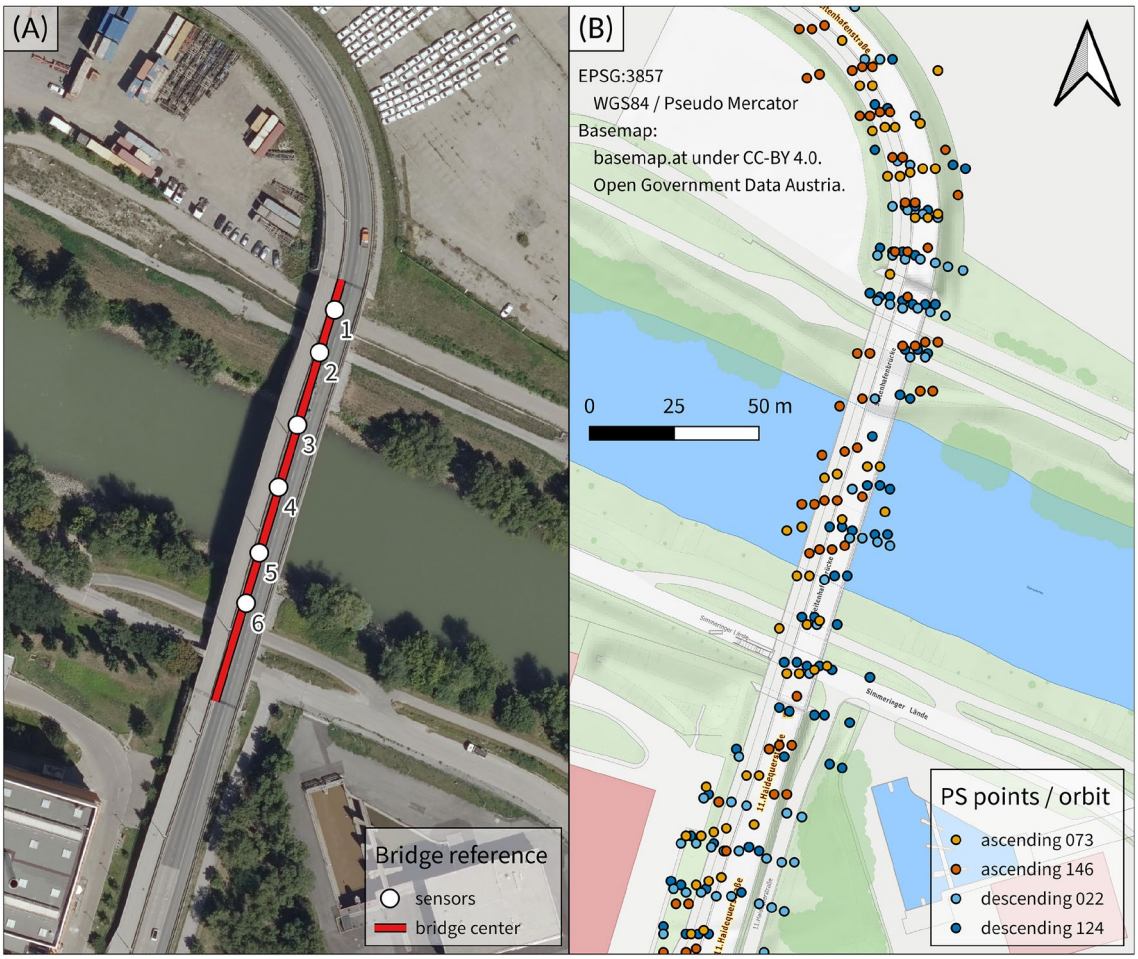

Fig. 3 **A** Location of the six water-level gauge deformation sensors (white dots) on *Seitenhafenbrücke* and the reference line of the longitudinal section of the bridge (red). **B** Location of PS-points in the area of interest. Colors correspond to the orbit numbers as used in Figs. 4 and 5

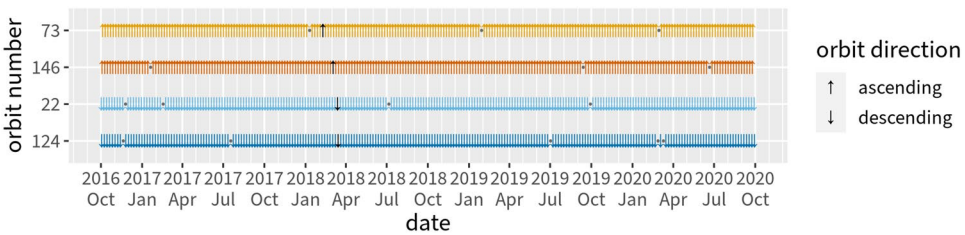

Fig. 4 Sensing dates of Sentinel-1 IW SLC data products used in this study. Colors correspond to the orbit numbers as used in Figs. 3 and 5. Black arrows indicate leader scenes, grey dots indicate missing scenes

Table 1 Overview of Sentinel-1 SLC data used in this study

Orbit direction	Orbit number	Incidence angle	Heading	Sensing time	Start date	End date	Images	Leader date	PS-points
Ascending	73	36.10	− 14.67	16:42 UTC	2016-10-05	2020-09-26	239	2018-02-09	51
Ascending	146	44.75	− 14.58	16:51 UTC	2016-10-04	2019-09-25	239	2018-03-04	78
Descending	22	32.82	− 165.37	05:09 UTC	2016-10-02	2019-09-29	239	2018-03-14	65
Descending	124	42.10	− 165.40	05:02 UTC	2016-10-03	2019-09-30	238	2018-03-15	79

The number of persistent scatterer (PS) points refers to the number of points within the area of interest as depicted in Fig. 3

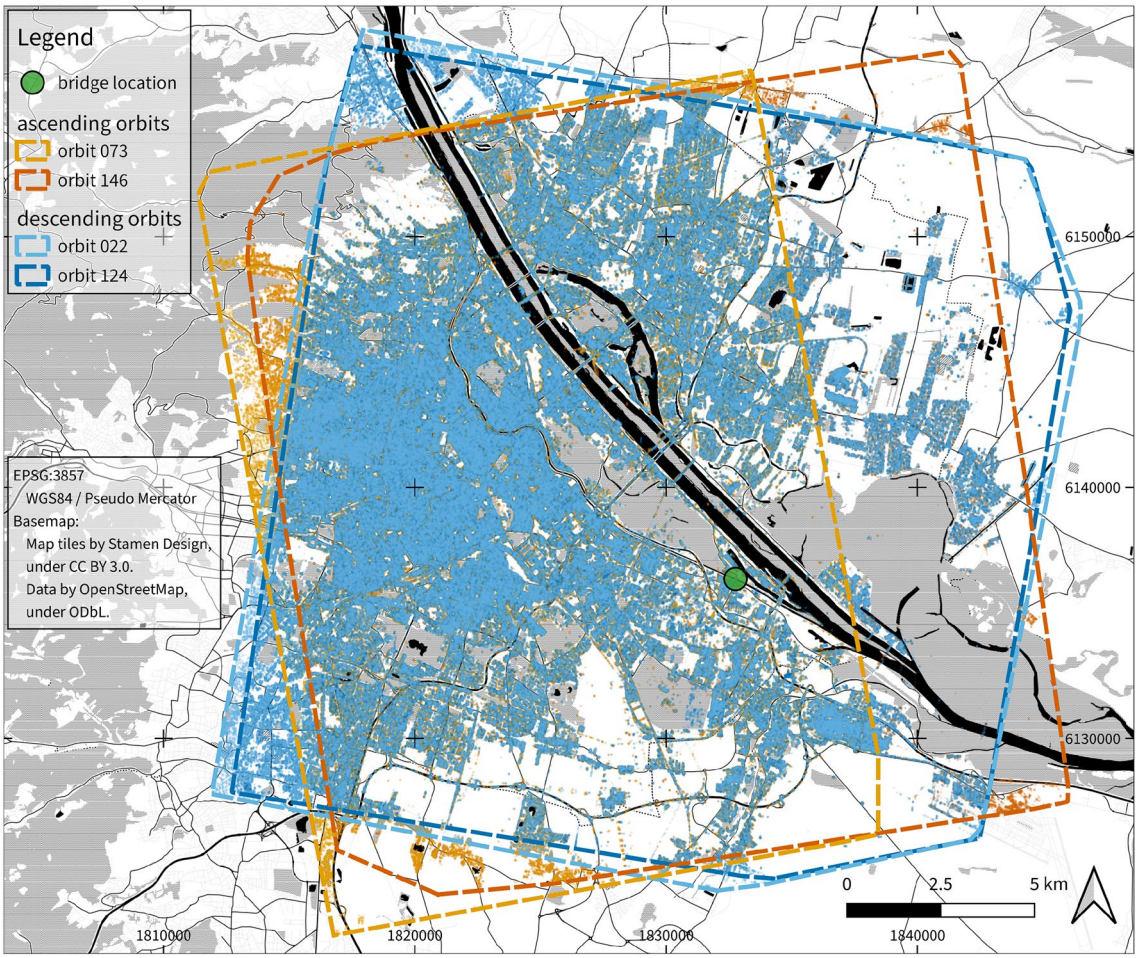

Fig. 5 Sentinel-1 orbits and PS-points over Vienna. The two orange polygons denote the two ascending orbits, the blue polygons denote the two descending orbits. Identified PS-points are signified in the respective orbit color. The green dot indicates the location of *Seitenhafenbrücke*

– *Persistent scatterer interferometry* The actual calculation of deformation time series was performed using the 'Stanford Method for Persistent Scatterers' as implemented in StaMPS/MTI (Hooper et al. 2012). The StaMPS processing chain includes the selection of pixels based on their noise characteristics, phase correction, phase unwrapping, and the removal of various error components from the phase. The mean of the whole area (per orbit) was used as a reference. The output is a deformation time series in line of sight for stable targets of opportunity, called persistent scatterer (PS) points.
– *Atmospheric correction of the deformation time series* The atmospheric phase contribution was mitigated by employing TRAIN, the 'Toolbox for Reducing Atmospheric InSAR Noise' (Bekaert et al. 2015), using data from GACOS, the 'Generic Atmospheric Correction Online Service for InSAR' (Yu et al. 2018).

The output of this first pipeline is time series of surface deformation for the identified persistent scatterers. Deformation is measured in relative to the leader scene in satellite line-of-sight for each of the considered orbits.

To improve the signal-to-noise ratio of the raw InSAR time series and to unveil underlying patterns more concisely, extensive post-processing steps were performed in a second pipeline:

– *Time series cleaning (outlier removal)* Extreme outliers were eliminated by employing robust STL (Seasonal decomposition of time series by LOESS, cf. Cleveland et al. (1990)) decomposition for seasonal series, and Friedman's Super Smoother (Friedman 1984) for non-seasonal series. Observation deviating by more than three times the interquartile range from the (possibly seasonally adjusted) smoothed value at the respective measurement time were replaced by means of linear interpolation (Hyndman and Khandakar 2008).

- *Time series smoothing* The cleaned time series were smoothed and interpolated on a daily basis, using locally weighted scatterplot smoothing (LOESS; c.f. Cleveland et al. 2017).
- *Bias correction for different sensing times* Due to the different sensing times of ascending (approximately 16:45 UTC) and descending (approximately 05:00 UTC) passes, a systematic error would be present in the satellite measurements when combining ascending and descending orbits. This error is rooted in seasonally dependent diurnal bridge deformation patterns occurring over the course of 1 day (Schlögl et al. 2021). To mitigate this bias, a correction term was applied for each day. This term is obtained by means of a random forest model (Wright and Ziegler 2017) linking the measured bridge deformation difference between the two sensing times to the prevailing environmental conditions at both sensing times. The (vertical) deformation difference (i.e. the target variable of the model) is derived from the in situ measurements recorded by the water-level gauge, and environmental conditions (i.e. the independent variables of the model) are represented by different weather variables, including air temperature, the zero degree isotherm, precipitation, relative humidity, global solar radiation, sunshine duration and wind speed. These weather data are available through the nowcasting system INCA, operated by the Austrian national weather service. By providing the meteorological data as input, resulting bridge deformation difference can be estimated for each day by using the predictions of the random forest model trained on available water-level gauge data. Please refer to Schlögl et al. (2021) for further details on the bias correction procedure.
- *Extraction of vertical and horizontal components from different orbit directions* Both the horizontal (east-west) and vertical (up-down) motion components were extracted from deformation values measured in the satellite's line-of-sight direction by combining the two descending and ascending orbits according to Eq. (1) (c.f. Delgado Blasco et al. 2019):

$$\begin{bmatrix} d_v \\ d_{h_{\mathrm{ALD}}{}^{\mathrm{dsc}}} \end{bmatrix} = \begin{bmatrix} \cos\theta^{\mathrm{asc}} & \frac{\sin\theta^{\mathrm{asc}}}{\cos\Delta\alpha} \\ \cos\theta^{\mathrm{dsc}} & \sin\theta^{\mathrm{dsc}} \end{bmatrix}^{-1} \times \begin{bmatrix} d_{\mathrm{LoS}}{}^{\mathrm{asc}} \\ d_{\mathrm{LoS}}{}^{\mathrm{dsc}} \end{bmatrix}, \qquad (1)$$

where d_{LoS} denotes the displacement along the satellite line-of-sight, d_v is the vertical displacement component and $d_{h_{\mathrm{ALD}}{}^{\mathrm{dsc}}}$ denotes the projection of the horizontal displacement in descending azimuth look direction (ALD). θ denotes the incidence angle and $\Delta\alpha$ is the satellite heading difference between ascending and descending orbit (c.f. Table 1). Horizontal and vertical deformation components were derived for an artificial grid, covering the bridge at a spatial resolution of 0.75 m × 0.75 m. For every grid point, the nearest PS points of any ascending and descending orbit located within a radius of 10 m were used for performing the conversion.
- *Time series clustering* To identify areas on the bridge where deformation patterns exhibit similar trajectories over time, both vertical and horizontal deformation series available at every grid point were grouped using longitudinal *k*-means clustering (Genolini et al. 2015).
- *Aggregation of results* Taking into account the proximity of in situ sensor locations to the deformation grid points as well as the information on the predominant cluster around the respective sensor location, ensembles of vertical bridge deformation were derived. These ensembles provide robust information on deformation patterns, which can be validated against the independent in situ measurements.
- *Time series decomposition* For each of these ensembles, the highly seasonal time series were separated into a seasonal component, a trend component, and a component indicating random noise. By eliminating seasonal and random components from the overall deformation, underlying trend patterns could be derived. This was again achieved using STL decomposition.
- *Creation of longitudinal profiles* To derive daily longitudinal profiles of bridge deformation, points were sampled at a spatial resolution of 1 m along the curb in the center of the bridge. Analogously to the in situ comparison described above, ensembles of vertical deformation were created by taking into account the proximity of each point sampled along the longitudinal profile to the deformation grid points as well as the information on the predominant cluster.

2.4 ALS

2.4.1 Data Acquisition System

The *4DU-Scanner* is a mobile mapping solution that can be carried by a car or UAV. The sensor integrates two time of flight LiDAR systems with 16 profiles each, i.e. 32 profiles are measured simultaneously with a maximum sampling rate of 600 k points per second and a maximum of two returns per echo (first/last). The system operates fully autonomous, integrating a *Trimble APX-15* UAV GNSS/IMU sensor for measuring position and orientation (i.e. the trajectory) during data acquisition. For capturing the *Seitenhafenbrücke*, the *4DU-Scanner* was carried by a *DJI Matrice 600 pro* UAV. To fulfill the Austrian regulation of the local aviation authorities, the UAV is equipped with a redundant dual flight-control. The maximum flight-time of this configuration is up to 15 min.

2.4.2 Data Collection

Two measurement campaigns have been carried out on 2020-04-09 and on 2020-10-21. During the first campaign, the side beam was captured at 9 am and at 3 pm, almost simultaneously to the MLS capturing with the RoadSTAR system (see Sect. 2.5.2). To capture both side beams of the bridge without crossing the bridge during flight (due to legal reasons), two flights were necessary for a complete capturing at one time. So all-together, four flights were carried out to capture the respective data. Each flight consists of several strips from different flight heights. The mean distance to the side beam is approximately 5 m.

For the April campaign, we aimed at capturing the downward facing side of the beam. Therefore, we started capturing with flight height below the object up to approximately 5 m above to cover the entire bridge. Figure 1 shows the sensor configuration at an average flight level along the side beam of the bridge. Figure 6 shows the point cloud and the therefrom derived mesh after co-registration and merging the data of the two morning flights of the first campaign.

For the campaign in October, a different flight pattern was chosen. To improve the quality of the trajectory (i.e. availability of GNSS-data) and to simplify the flight-operation, several strips enabling the capturing of the side beam from top have been carried out. The flight-time for this pattern was 3 min to capture the Western side beam. The Eastern side beam was not clearly visible from top due to various constructions and a significant layer of dirt. So altogether, three independent observations of the Western side beam at different weather conditions (morning/afternoon; spring/fall) were used for the deformation analysis as described in the following section. The achievable accuracy with respect to water-level gauge reference data is evaluated in Sect. 3.2.

2.4.3 Data Processing

Based on GNSS and IMU data and using a local reference station (APOS correction data, (BEV 2022)), a high-quality trajectory has been calculated using the post-processing-kinematic (PPK) principle (Puente et al. 2013). The data have been transformed into ETRS89/UTM 33N projection (EPSG:25833) and locally referenced with respect to reference points provided by the Bundesamt für Eich- und Vermessungswesen (BEV-Austrian federal office for surveying). The resulting absolute accuracy is ± 5 cm. To improve the local accuracy of the data, our first approach aimed at local co-registration of the individual flight-strips using the iterative closes point (ICP) method (Besl and McKay 1992). To minimise the measurement noise, a sophisticated approach described by Nothegger (2011) has been applied. The core idea is to investigate the local neigbourhood of a point. Based on a local density estimation, the resulting point is shifted to the highest density of its neighboring points along a robustly estimated local surface normal. Figure 6 shows the resulting point cloud and the therefrom derived 3D-triangulation mesh. The local accuracy of the resulting model was ± 2 cm. Considering the expected deformation of the bridge, this was still not sufficient.

To increase the accuracy of the resulting profile describing the side beam, we localised the modelling approach further; i.e. we defined a vertical reference plane intersecting the side-beam. For each flight strip, we extracted points within a certain distance to this reference plane, projected them into a 2D-reference system, fit natural cubic 2D-splines into each of these point clouds and finally calculated an average profile-spline based on all the individual profiles. The spline describing knots were defined with 10 m distance. This was done for all available datasets, i.e. morning and afternoon acquisition of Eastern and Western side-beam of the April campaign and western side beam of the October campaign.

2.5 MLS

2.5.1 Data Acquisition System

In addition to the UAV-based measurements using ALS, data acquisition on *Seitenhafenbrücke* was also carried out using a truck-mounted mobile mapping device. Originating from network wide data collection of road surface properties, the mobile laboratory RoadSTAR (see Fig. 1) records numerous relevant surface parameters of a roadway in a single pass. These parameters include skid resistance, longitudinal and transverse evenness and macro texture.

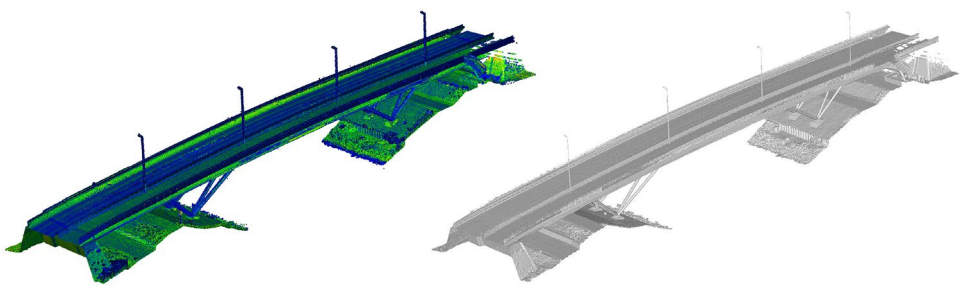

Fig. 6 UAV-ALS measurements from the morning flight on April 9th, 2020. The image shows the ALS point cloud (left) and the derived mesh (right)

Fig. 7 Left: the Fraunhofer PPS profile scanner. Right: the Applanix POS LV420 dead reckoning system

While RoadSTAR was designed to capture the pavement surface, its range is in many cases sufficient to capture also parts of the edge beam surface. To allow this, RoadSTAR needs to drive close to the edge beam, while the space between laser scanners and edge beam must not be obscured (e.g. by a vehicle restraint system).

For the task at hand, the Fraunhofer PPS profile scanner (see Fig. 7, left) was used to record the surface of the roadway or pavement. The profile scanner is mounted on the front of the vehicle and covers a width on the ground of 4 m with 800 profiles per second. The point spacing in the transverse direction is approximately 5 mm. The measurement uncertainty σ (i.e. 1 standard deviation) is given as 0.15 mm for 100 points on a surface with a reflectance of 80%. An Applanix POS LV420 dead reckoning system is used for positioning and attitude determination (cf. Fig. 7, right). For post-processing of the trajectory, virtual reference stations were created by EPOSA (EPOSA 2022) in the immediate vicinity of the surveyed bridge.

The RoadSTAR data acquisition is limited to the surface of the bridge, which typically has a pavement (often mastic asphalt or SMA) applied to it, which may have a different deformation behaviour from the bridge.

2.5.2 Data Collection

To capture the full diurnal variations of the temperature-caused bridge deformations, measurements were conducted on 2020-04-09 from 08:05 to 09:17 and from 14:30 to 15:35. The bridge has two lanes, so two runs were necessary to cover the full width of the bridge. Four runs were done in each direction in the morning and two runs in each direction in the afternoon. The distance between the two abutments is approximately 135 m. The vehicle speed was between 30 and 40 km/h.

2.5.3 Data Processing

In the first step, the recorded trajectory of the positioning and attitude system was post-processed. Therefore, RINEX data of a virtual reference station, created by service provider EPOSA (EPOSA 2022), was used together with the recorded data of the GNSS receivers, the IMU and the DMI data. The result is the 'Smoothed Best Estimate Trajectory' (SBET) of the driven paths including the attitude of the measurement system over the bridge. The SBET was exported in ETRS89/UTM 33N coordinate system. The resolution of the SBET is 200 Hz, which corresponds to approximately 5 cm on the ground.

From the SBET and the recorded laser scanner data, point clouds were calculated for each pass over the bridge. This results in one LAZ file per pass. To remove inevitable measurement inaccuracies of the trajectory, the resulting point clouds have been aligned. Therefore, spots in the area of the north and south abutment of the bridge were identified in the point clouds. These two points lie on the abutment and cannot move due to changing temperature.

Subsequently, all point clouds were translated to have an identical northern reference point. Afterwards, the point clouds were scaled in x, y and z direction so that the point clouds share the same identical southern reference point. The translations and the scaling were in the range of 10 cm. Using this method, the height variations along the bridge were preserved.

Through the aligned point clouds, 16 longitudinal profiles were fitted along the bridge with a transversal spacing of 0.5 m, 8 in southbound, 8 in northbound direction (Fig. 8). The profiles have a longitudinal sampling of 1 m. Due to the alignment of the measurement runs, the longitudinal profiles cut the bridge at identical locations and for all further comparisons, only the z-coordinate of the points has to be considered. Each profile was then averaged separately for all morning and all afternoon trips.

2.6 Temperature

The change of weather conditions between consecutive measurements might cause significant changes of the bridge deformation that have to be compensated. To avoid using any sensors mounted on the bridge to measure the on-site temperature, a finite element method was applied. It uses solely the available meteorological data: air temperature,

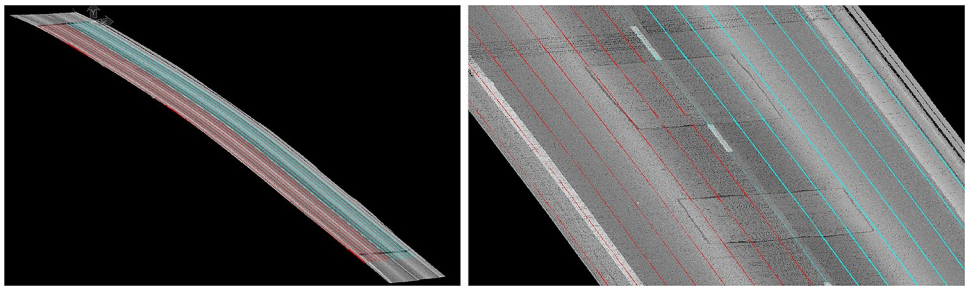

Fig. 8 Left: fitted longitudinal profiles on the bridge deck. Red lines signify profiles in southbound direction, cyan lines show profiles in northbound direction. Right: detail of longitudinal profiles running on the bridge deck surface

wind speed and solar radiation (recalculated from sunshine duration per hour) and allows determination of effective temperature gradient (T_G) and the uniform temperature (T_u) at a given time. These parameters are the most suitable for further application as the temperature loads on a commonly used beam model of the bridge (Sanio et al. 2017). Temperature related deformations calculated in such a way are subtracted from the deformation measurements. In case of statically determined bridges, the temperature induced deformations ($w_{\Delta T}$) for all longitudinal coordinates x can be calculated directly using Eq. (2), with the only uncertainty being expansion coefficient α_t (Zhou et al. 2021):

$$w_{\Delta T} = \frac{\Delta T_G \cdot \alpha_t \cdot x}{2 \cdot \text{height}} \cdot (x - \text{length}) \tag{2}$$

3 Results

3.1 InSAR

Both vertical and horizontal deformation component series are based on the deformation results of the prevailing cluster around the in situ measurement locations. By considering the time series of all corresponding persistent scatterers, the resulting ensembles do not only provide single point measurements, but also some indication about the measurement uncertainty. Consequently, results are presented as ensemble average (i.e. arithmetic mean) and ensemble range (i.e. minimum and maximum) for the six ensembles around the in situ measurement locations of the water-level gauge deformation sensors.

3.1.1 Vertical Deformation

The main advantage of assessing the vertical deformation component is the possibility to validate the results with accurate in situ measurements. Overall results of the satellite-based vertical deformation monitoring are remarkably accurate (Fig. 9). This is especially true for the southern part of the bridge (sensors S5 and S6) as well as the northern middle part of the bridge (sensor S3), where the mean absolute deviation between the two measurements is less than 2 mm (Fig. 10). Results for the center of the bridge (sensor S4) indicate an underestimation of the actual deformation. While the mean absolute deviation is around 5 mm, the maximum underestimation is up to more than 10 mm in winter and close to 8 mm in summer. The northern part of the bridge yields somewhat inconsistent results, as satellite measurements suggest virtually anticyclic deformation patterns as opposed to the measured bridge deformation. Mean absolute deviation between the two measurements ranges between 3 mm (sensor S2) and 4 mm (sensor S1).

3.1.2 Horizontal Deformation

Horizontal deformation is reported with respect to the azimuth look direction of the satellite sensor on a descending orbit. This corresponds almost perfectly to movements along the lateral axis of the bridge, as the ALD of the respective descending Sentinel-1 orbits exhibits a clockwise shift of 14.6° from an east-west axis. At the same time, *Seitenhafenbrücke* is oriented from ENE to WSW, which results in the descending ALD being nearly orthogonal to the bridge orientation. Overall, the horizontal deformation components are less pronounced than the vertical ones. A summary of the deformation ensembles around the in situ sensor locations shows diametrically opposed movement patterns for most locations (Fig. 11). This is consistent with expected bridge expansion in summer and contraction in winter, and becomes clearer when considering the spatial location of deformation clusters (Fig. 12). Points belonging to the violet cluster are located on the western side of the bridge, and exhibit a seasonal movement of 5 mm towards west in summer, and 5 mm towards east in winter, resulting in an absolute annual deformation range of 1 cm. The opposite applies to PSI points in the blue cluster, which are located on the eastern side of the bridge and move towards east in summer and back towards west in winter. The green and red clusters are difficult to interpret, as they show no consistent

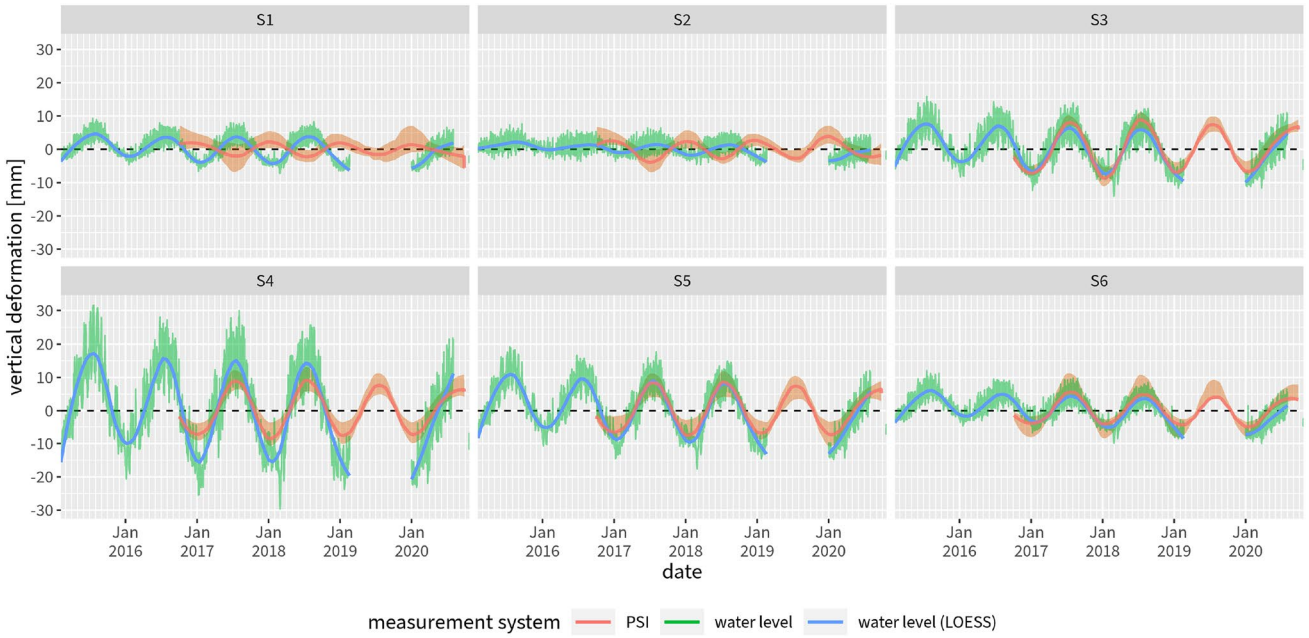

Fig. 9 Comparison of vertical bridge deformation patterns between in situ measurements and InSAR-based measurements for all six water-level gauge sensors on the bridge. In situ measurements are displayed as original measurements (green) and a smoothed version (using local regression) of these measurements (blue). Results for the PSI time series are displayed as summary of the whole ensemble: The orange line shows the mean deformation across all chosen InSAR PS points, the shaded area displays the deformation range of the respective ensembles

picture. Some members of the green cluster (e.g. around sensors S2, S3 and S6) could be considered a slightly less pronounced version of the movement patterns in the blue cluster. The red cluster, however, is basically noise that occurs on the southern and northern bridge ramps rather than directly on the bridge.

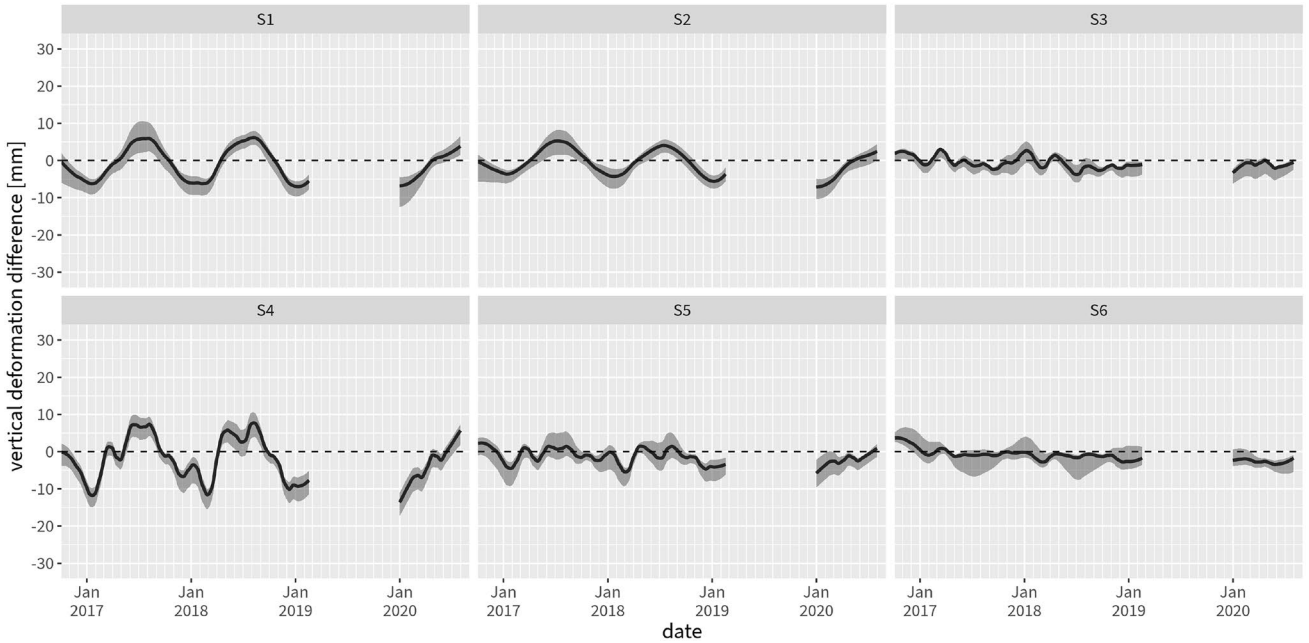

Fig. 10 Difference between in situ measurements and InSAR-based measurements of vertical deformation for all six water-level gauge sensors on the bridge. The black line shows the mean deformation difference across all chosen InSAR PS points, the shaded area displays the range of the difference in the respective ensembles

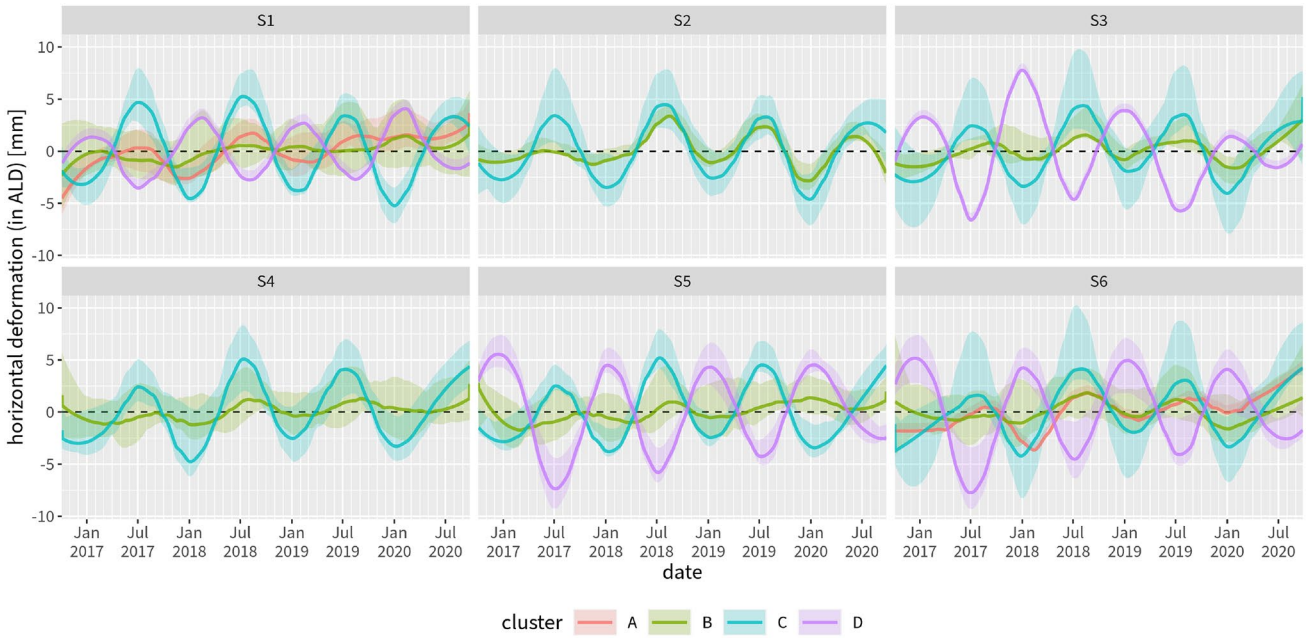

Fig. 11 InSAR-based measurements of the horizontal deformation component in azimuth-look-direction, summarised around the six water-level gauge sensors on the bridge. The solid lines show the mean deformation difference across all chosen InSAR PS points, the shaded area displays the range of the difference in the respective ensembles. Colors signify the four clusters derived via longitudinal *k*-means clustering (c.f. Fig. 12). Positive values correspond to eastward movement, negative values indicate westward movement

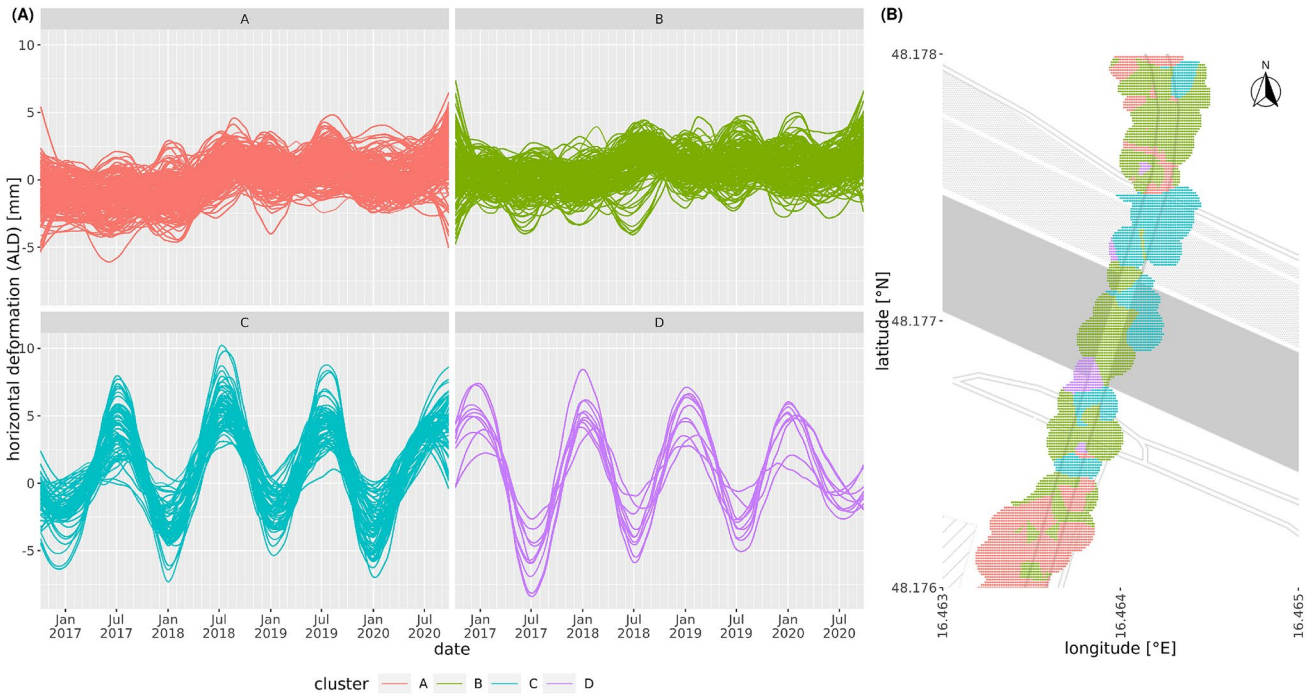

Fig. 12 Time series clusters for horizontal deformation component obtained via longitudinal *k*-means clustering of the deformation time series (**A**) and corresponding location of cluster points on the bridge (**B**). Positive values correspond to eastward movement, negative values indicate westward movement

3.2 ALS

To evaluate the achievable accuracy of our approach, we investigated the extracted, spline-based profiles in comparison to ground-truth data determined by the water-level gauge. Figure 13 shows the height differences between the profiles approximated for the Western edge beam for all three ALS-campaigns (April morning and afternoon and October). As described in Sect. 2.4.2, during the first campaign, we aimed at capturing the bottom side of the edge beam. This limited the area that could be captured due to the minimum flight height above the ground to avoid hitting obstacles. Therefore, the area between reference point S2 and S5 (approximately 60 m of the bridge construction) has been evaluated. As height reference, S2 was selected, i.e. the profiles were set to identical height at these points resulting in a height difference of 0 mm.

The solid lines represent the measured differences between the profiles at the different timestamps while the dotted line show the difference of the reference data determined by the water-level gauge at the reference points S2–S5. We can see that the relative trend can be determined properly for all three measurements. The significantly higher variation at S3 can probably be explained by the fact that the October campaign aimed at measuring the upper side of the side beam, i.e. a minor variation of the construction may have influenced the result as this peak is not detected when comparing the two measurements of April, both capturing the downward facing side.

3.3 MLS

Figure 14 shows an example of the height curves of the averaged profiles for the southbound direction, with relative heights in [mm] from the northern reference point shown here. In addition, the range of relative heights in [mm] is given for each reference point. The curves show a consistent picture with ranges in the range of 1–6 mm. The locations with larger ranges are located at gullies that are situated at the edge of the bridge deck. In these locations, the profile fitting of the surface leads to larger variations between profiles.

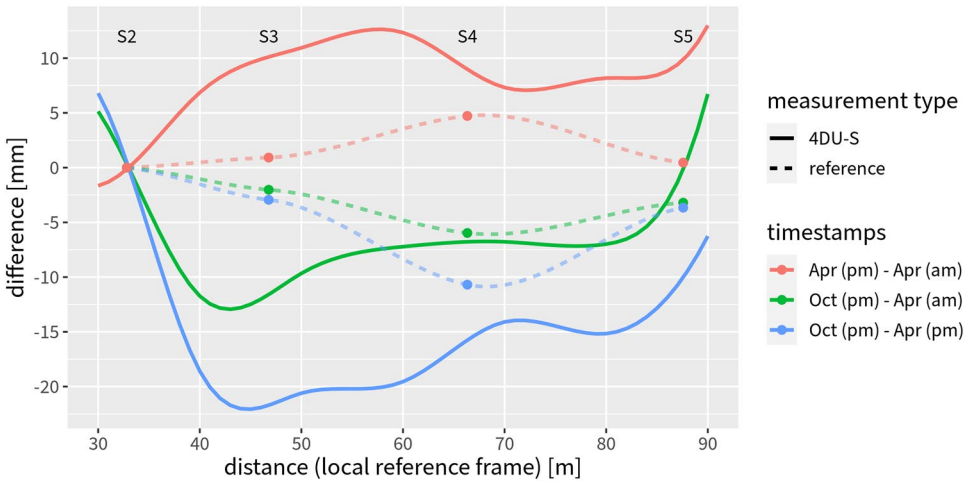

Fig. 13 Comparison of ALS-based deformation differences with reference in situ measurements. Note that reference measurements are interpolated using simple X-splines (dashed lines) to visually aid in the comparison of ALS and in situ measurements

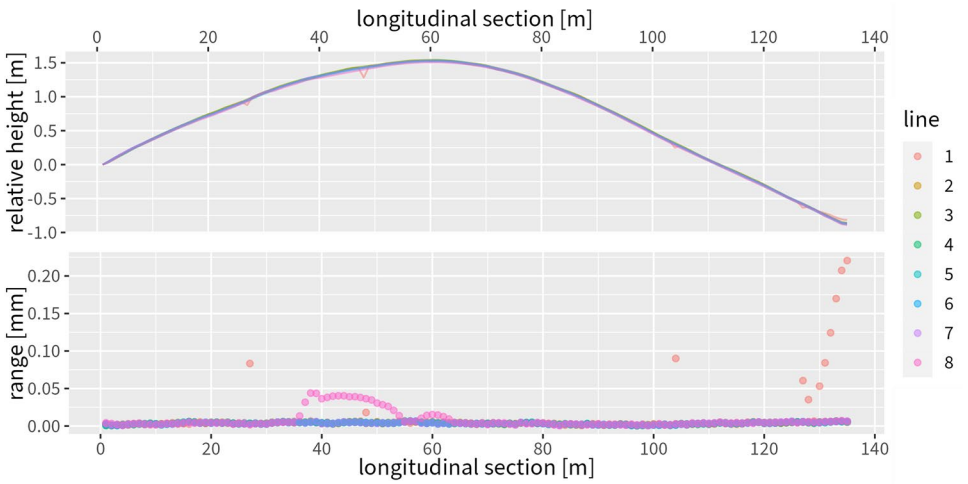

Fig. 14 Average relative height of the approximated lines for all morning measurements (top) and ranges of the relative heights at the of the supporting points of the lines (bottom)

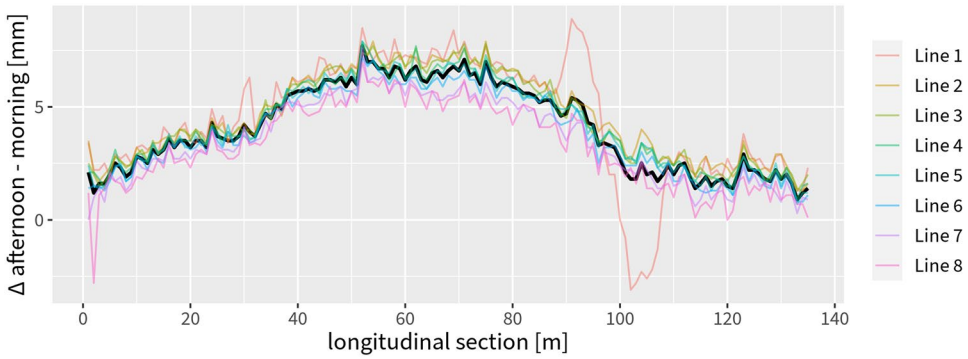

Fig. 15 Height differences between afternoon and morning for each of the 8 lines of the southbound direction. The thick black line shows the average deformation

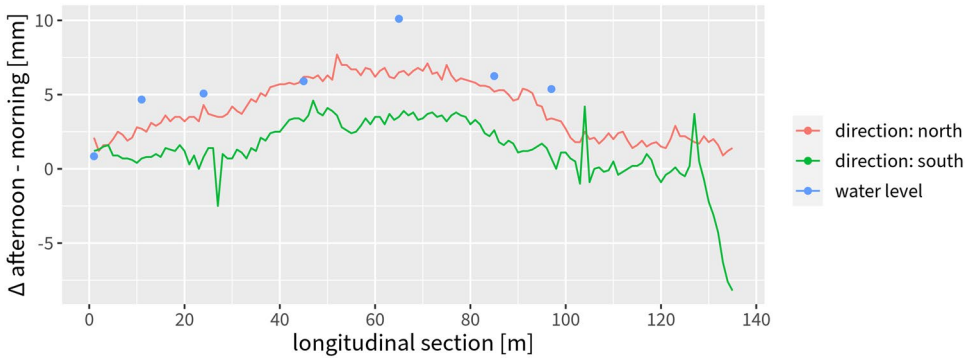

Fig. 16 Comparison of daily deformation differences between afternoon and morning. Blue dots show the measurements taken at the locations of the water-level gauge. Lines show deformation differences obtained via mobile laser scanning, displayed as average across the 8 lines of each direction

Differences for each of the 16 averaged morning and afternoon profiles show a consistent picture. Under the justified assumption that the deformations of the bridge and the asphalt surface are identical during the day, this represents the deformation of the bridge in the (spatial) area of the respective line.

Assuming that the deformation of the bridge in the transverse direction remains the same, i.e. no torsion occurs, the differences of the individual lines can be averaged. This was done for both the northbound and southbound directions. Figure 15 shows the height differences between morning and afternoon for each of the 8 lines of the southbound direction as well as the averaged deformation (thick black line).

Figure 16 shows the average height differences in the transverse direction between morning and afternoon for both directions of travel. In addition, the height differences of the electronic water-level gauge sensors are shown as blue dots, which result in the average of the measurement periods of the laser scans in the morning and afternoon. In the northbound direction, the agreement with the differences from the electronic water-level gauge is high except for the fifth point.

Table 2 shows the deviations between the water-level gauge and the mobile mapping measurement for both directions. The average deviation in southbound direction is 3.6 mm, in northbound direction it is 1.1 mm.

Table 2 Difference Δ showing the daily variation (morning-afternoon) between the water-level gauge measurements (sensors and corresponding location) and the RoadSTAR measurements, at the stations of the water-level gauge sensors

Sensor	Location [m]	Δ direction: South [mm]	Δ direction: North [mm]
S0	1	− 0.4	− 1.2
S1	11	4.0	2.0
S2	24	4.3	0.8
S3	45	2.7	− 0.3
S4	65	6.6	3.6
S5	85	3.7	1.1
S6	97	4.7	1.9
	Average	3.6	1.1

3.4 Temperature

Using the existing monitoring system on *Seitenhafenbrücke* the proposed method for a temperature induced displacement was estimated and validated over 2 years with a timestep of one hour (Fig. 20). The bridge cross section was modelled with 2d elements and loaded on all outer sides with the air temperature, with respect to the convection coefficient, and with sun radiation applied on the upper surface including its reflection property. Resulting surface temperatures were compared to two

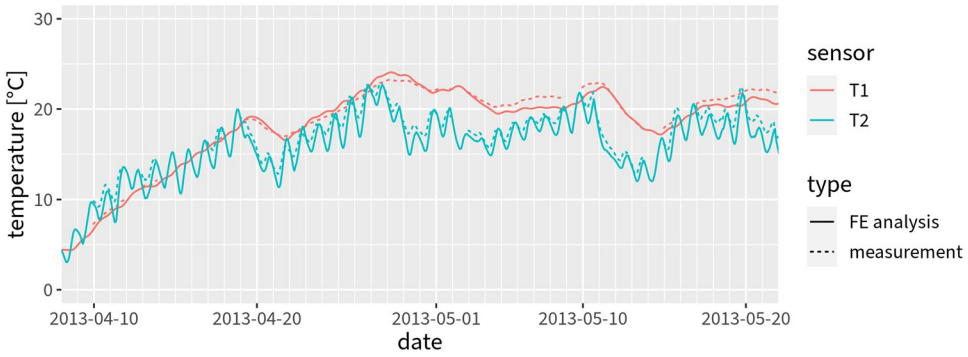

Fig. 17 Comparison between measured and FE-based temperature of *Seitenhafenbrücke*

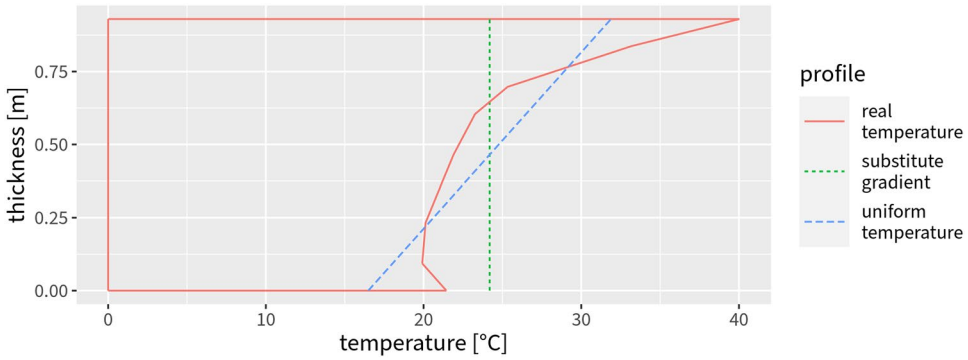

Fig. 18 Temperature distribution and recalculated uniform temperature and linear gradient for 2013-05-01 15:00

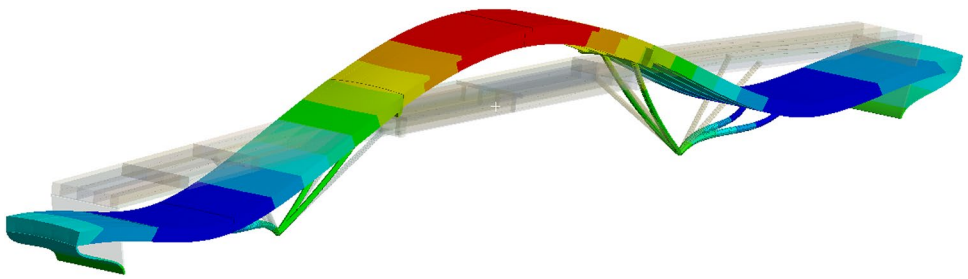

Fig. 19 FE model of *Seitenhafenbrücke* showing temperature induced deformation

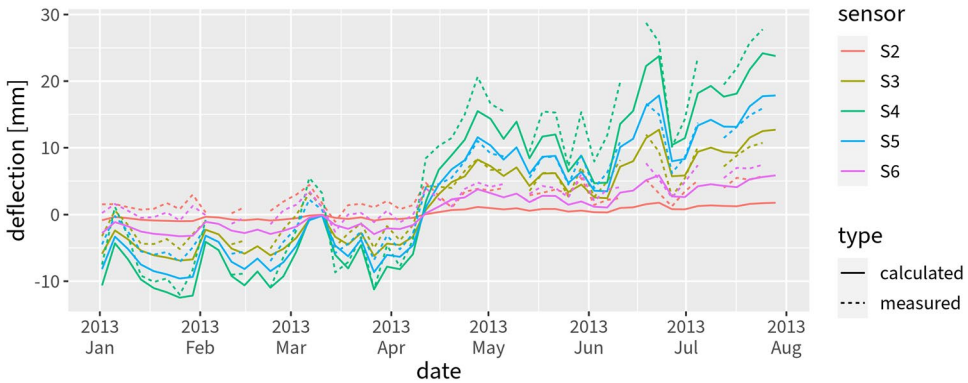

Fig. 20 Comparison between measured (dashed) and modelled (solid line) bridge deformations in time

temperature sensors mounted on the lower side of the bridge surface (Fig. 17). The standard deviation of the differences was equal to 1.34 °C. After obtaining the temperature distribution over the cross section, the uniform temperature and the linear gradient could be calculated (Fig. 18).

As *Seitenhafenbrücke* is statically undetermined, a beam FE model of the bridge was needed to calculate the temperature induced deformation (Fig. 19). In this case, a soil–structure interaction contributed to the vertical deformation as it affected the bridge elongation. Therefore a model update was needed to achieve the same behaviour observed in the measurement. In case no monitoring system was mounted, this would have led to the need for several consecutive deformation measurements to obtain the deformation pattern. Upon correcting for this deformation component, a prediction with a standard deviation of 2.3 mm was achieved across all mounted sensors (Fig. 20).

4 Discussion

4.1 InSAR

Despite the relatively low spatial resolution as well as various measurement uncertainties, which thwart reaching millimetric accuracy (that could be achieved in theory) in this practical example, results underline the potential of InSAR for continuous long-term monitoring of engineering structures. Especially, the monitoring of long-term deformation patterns and the detection of potential movement trends are promising application areas. In the case of *Seitenhafenbrücke* the overall seasonality is captured quite well. In cases of extreme seasonal deformation, the InSAR based measurements tend to underestimate the displacement rate in some cases. To some extent, this is likely due to the time series smoothing applied during the post-processing. While LOESS (or other filtering methods for that matter) is useful for decreasing noise and thus obtaining more robust results, it could to some extent amplify the underestimation of peak deformation rates in time series exhibiting strong seasonality.

The actual quality of the obtainable results is strongly dependent on the recording geometry and local conditions (Schlögl et al. 2022). Taking bridges as an example, this specifically concerns the following aspects:

- The orientation of the bridge: An orientation which faces approximately north–south—i.e. in the satellite flight direction—is usually more favorable than an east-west orientation, because potentially more scatterers or reflectors are available. In addition, the sensitivity for displacements occurring horizontally in North–South direction is very limited due to the viewing geometry on sun-synchronous orbits.
- The surroundings of the bridge: Objects in densely built-up areas are more difficult to analyse than bridges in the proverbial ‘green field’. This is due to the high backscatter intensity in built-up areas, which complicates the measurement of object-specific deformation signals.
- The height of the bridge above ground level: The higher a bridge is above ground level (i.e. the digital elevation model used in the processing), the more difficult it is to precisely geolocate the PS points.
- The location of the bridge in the terrain: Effects caused by pronounced topography, such as layover or radar shadow, complicate analyses in mountainous terrain.

Since Sentinel-1 InSAR data are freely available, InSAR-based deformation analyses are a cost-effective method for long-term monitoring of engineering structures. Continuous monitoring of infrastructure assets can potentially be provided over large areas (e.g. network wide) with weekly updates and sub-centimetric accuracy. At the same time, there are three main issues that render a broad application of this method somewhat cumbersome. First, solid expertise in radar remote sensing is required to conduct multitemporal interferometric analysis. Second, depending on the area of interest and the update frequency, potentially substantial processing resources are needed for analysing large stacks of SLC data sets. Third, the extensive post-processing of time series that is necessary to obtain robust and interpretable results from deformations in satellite line-of-sight does not make the preparation of PSI data a straightforward endeavor.

Employing the mean of the whole area as a reference instead of using a dedicated reference point might introduce uncertainties caused by possible surface displacements within the area, as well as errors in tropospheric correction due to atmospheric variability. To some extent, this is a trade-off between optimising the processing towards high accuracy for single structures, and covering larger areas, e.g. in whole cities.

Open issues where further research is needed to translate deformation monitoring of infrastructure assets into practical applications specifically relate to three main aspects. First, uncertainties which stem from, e.g. atmospheric effects or artifacts of phase-unwrapping problems need to be tackled and reduced further. Second, further developments in statistical post-processing of time series are required. The processing chain described here leads to a slight underestimation of certain deformation patterns. To increase the robustness of the results, reductions in the accuracy of the deformation measurements in the summer maximum and winter minimum in the middle of the bridge were accepted to some extent. Third, the development of algorithms for the detection of abnormal behavior are considered a crucial issue for future work with high potential. The overall aim has to be to move from ex post analysis showing deformation patterns in hindsight towards automated early warning systems that issue warnings proactively.

4.2 ALS

Basically, the achievable accuracy of the UAV-based application of LiDAR sensors is limited by three factors:

- Accuracy and precision of the LiDAR sensor,
- Accuracy of the sensor used for georeferencing (GNSS/IMU sensor),
- Availability and quality of stable reference points.

The *4DU-Scanner* integrates two *Velodyne Puck* LiDAR sensors. The range accuracy of this sensor is ±30 mm comprising measurement noise and angle measurement errors due to lack in calibration. The RMS of the positioning error of the *Applanix APX-15* GNSS/IMU sensor is specified with 20–50 mm under optimum conditions. Especially for the April campaign, aiming at flight heights below the bridge level causing varying visibility of available satellites, it has to be expected that the quality of the trajectory is below this expectations. Reference points have not been available. Aiming at fast and efficient measurement solutions, the establishment of a geodetic network based on stabilised marker points is unrealistic. In addition, such points may be realised only at stable parts of the construction. In our case, such points would not support the quality of the inspected area of the bridge.

Considering these circumstances and studying related work shows, that the typical achievable total error budget after registration and strip-adjustment of such systems is approximately ±50 mm. By means of the described procedure of localising the problem and using a high degree of redundancy with respect to the number of 'independent' measurements, we were able to determine at least the relative deformation trend with respect to the different thermal conditions of the bridge. The deformation was overestimated (approximately factor 2; 5–10 mm differences) and only a limited area of the bridge could be investigated due to restrictions in safe flight operation (distance to ground).

4.3 MLS

The investigation of the error budget of the mobile mapping system shows two essential components: on the one hand, the measurement uncertainty of the laser scanner with less than 1 mm, on the other hand, the positioning and angle determination with dead reckoning. The position error—and in this case of particular interest—the height error is strongly dependent on the reception conditions and in the best case is in the order of 2–3 cm. The inclusion of IMU data naturally leads to stabilisation, which has a positive effect on the consistency of the results. However, position and attitude remain the main sources of measurement uncertainty. Considering this, the results from the comparison with the results of the electronic water-level gauge with differences between 0 and 6 mm are remarkable. The diurnal variation of bridges is in the range of millimetres. Additional measurements are necessary to investigate how repeatable the results of mobile mapping are and more automation is needed to facilitate the process from raw measurement data to the deformation result.

4.4 Temperature

Estimating the bridge temperature based on weather data and an FE Model introduces a minor degree of uncertainty in comparison to the mounted sensors. The big advantage is, however, that the outcome determines exactly the parameters needed for temperature compensation instead of the usually measured surface temperature. Therefore, the results obtained through this method can rather be considered superior to the sensor-based data, despite the slightly higher uncertainty. Statically determined bridges experience expansion in the longitudinal direction (due to uniform temperature) and curvature of the cross section over height (due to the temperature gradient). The first one is unimportant for the purpose of deformation compensation, the latter is only related to the expansion coefficient. For statically indeterminate bridges such as *Seitenhafenbrücke*, the two components act simultaneously and the effectiveness of the temperature compensation depends mostly on the accuracy of the FE model. It should be noted that with increasing number of measurements, the uncertainties of temperature compensation can be reduced. An important issue is the deformation pattern, which is usually different for temperature loading and damage-induced deformation of the bridge.

4.5 Comparison

The three different remote sensing measurement techniques described here are substantially different in terms of methodology, accuracy as well as temporal and spatial resolution. Consequently, each of these methods does have its own benefits and limitations, and their practicability is dependent on the context and the intended purpose of the monitoring.

The biggest advantages of satellite-based InSAR analyses are the possibility to cover large areas (i.e. the whole network), the high temporal resolution, and the low invasivity in terms of traffic interruptions. In addition, retrospective analyses are possible, as long as InSAR data covering the area are available and the viewing geometry of the bridge allows for the detection of persistent scatterers. These benefits come at the cost of reduced accuracy in practice, especially in case of heavy traffic and during challenging atmospheric conditions. In addition, the quality of achievable results is dependent on the type of object under consideration, the viewing geometry, and the topography of the surroundings. While

this entails that the InSAR method will not work equally well for all bridges, or even might not work at all in some unfavourable cases, this problem can be alleviated to some extent using artificial corner reflectors (Selvakumaran et al. 2019). It should also be noted that InSAR analyses require a rather complex processing pipeline as well as substantial computational resources for processing and storing data. In addition, the interpretation of results is not always straightforward for people unfamiliar with SAR remote sensing, for instance if deformations are reported in satellite line-of-sight. While recent endeavors related to the establishment of a European Ground Motion Service (Crosetto et al. 2020), the implementation of national ground motion services as well as the processing on demand services (such as ESA's Geohazard Thematic Exploitation Platform) have substantially lowered the entry barrier and facilitated the access to InSAR data for a broader community, results obtained at continental or country scale do need to be handled with care when seeking to assess specific objects. Thus, InSAR is recommended for (either continuous or retrospective) long-term monitoring, and for the assessment of general trends. Next steps should focus on enhancing continuous monitoring towards early warning applications, which could then trigger a more detailed scrutiny in case unusual deformation patterns are detected.

Among the presented methods, ALS provides the highest flexibility concerning the accessibility of the area of interest of a bridge. Considering the construction of the *Seitenhafenbrücke*, the shape of the edge beam has the highest probability to represent the current shape of the bridge; i.e. a deformation of the bridge can be observed most reliably, if capturing and modelling the edge beam at different dates and derive the respective deformation model. While InSAR models are derived from distinct points which are dependent on the bridge geometry and MLS-based data acquisition, if applied as described within this article, is limited to the area close to the vehicle, the UAV, used for ALS, may generally be directed to any viewing position to capture the desired structure. However, it turned out that the configuration of the flight path, especially the potential limitation of available GNSS signals for precise positioning as well as the incidence angle of the emitted laser beams for distance measurement, limits the achievable accuracy of this approach. Therefore, proper planning of the UAV mission is of crucial importance to achieve the best results possible. Compared to the MLS approach, the absolute accuracy of ALS is lower due to the restrictions introduced by the limited size and weight of the georeferencing sensors that can be applied by UAV. However, the relative trend of the model deformation, observed at different timestamps, could be determined with the described approach.

The broader idea behind the use of MLS for deformation measurement is that valid data about the deformation of many bridge objects distributed over the network can be obtained, which are collected in the context of network-wide road condition surveys. Through recurring, network-wide inspections, a time series for many non-instrumented bridges could be obtained without additional measurement effort. During network surveying, the day and time a certain bridge is passed is not determined beforehand, therefore it cannot be guaranteed that environmental conditions of two runs are comparable. Hence, it is necessary to integrate a temperature-deformation model for each bridge in order to compensate for different ambient temperatures. Over longer periods of time—the inspection intervals for network-wide condition monitoring are usually 4–5 years—it cannot be safely assumed that the bridge deck pavement will undergo the same deformations as the bridge structure itself. As shown at the example of *Seitenhafenbrücke*, averaging over several lines along the structure seems beneficial in mitigating this issue. This avoids that shoving or delamination in the wheel tracks leads to incorrect deformations. For economic reasons, it does not seem feasible to interrupt the road condition survey runs at each bridge to gather additional data through repeated measurements. Therefore, a trial on a bridge (ideally an instrumented one) over a longer period (e.g. 3 years) with single measurements every month would be beneficial to get sound evidence on the potential of using just single runs. On the plus side, the mobile mapping systems provides a wealth of additional data on the condition of the bridge deck (e.g. ruts, surface defects, guard rail, etc.) which are beneficial for bridge maintenance planning.

5 Conclusions

This article presents three remote sensing technologies for contactless measurement of bridge deformation. The performance of each method is evaluated in comparison to a fixed monitoring system, and merits as well as limitations are discussed. Results show that all methods are well capable of detecting general deformation trends, albeit exhibiting different stages of maturity.

The main application of InSAR lies in long-term continuous deformation measurement of the overall structure. In theory, large areas can be covered at low cost, and at quite frequent update intervals (e.g. once per week in case of Sentinel-1). However, certain limitations and challenges do currently remain when it comes to the practical application, at least with respect to frequent updates over large areas. Some challenges pertain to the exact estimation of certain phase components (e.g. atmospheric phase contribution), the viewing geometry in complex terrain, the geometry of the object under consideration, and the potential underestimation of horizontal and vertical deformation components in case of pronounced seasonal deformation

patterns. However, InSAR can definitely provide added value for the long-term monitoring of engineering structures, especially if retrospective analyses are desired.

Among the described approaches, ALS based on UAVs is the most flexible one with low acquisition costs compared to the described mobile mapping MLS approach, and low application and processing demands compared to InSAR. However, due to its limitations with respect to size and weight of the payload, the achievable accuracy is limited as well. Nevertheless, we were able to determine the deformation trend when comparing the three measurement campaigns to the ground-truth data. Hence, this method is well suited to be applied complementary to the two other approaches, for small and hardly accessible objects, or in case of lower accuracy requirements.

Mobile mapping as presented in this paper can be conducted during regular measurement campaigns. MLS-based deformation measurements can be derived as 'by-products' of recurring network-wide inspections. After post-processing, the derived deformations are in a similar range as provided by the reference. More research is needed on the required number of repeated measurements to get valid results and detect outliers reliably. This is a crucial point for application in practice, as repeated runs at each bridge would impede the original purpose of network surveying.

In the current stage of development, all three remote sensing methods are suitable for supplementing current structural condition assessments rather than replacing proven methods such as bridge inspections or water-level gauge measurements.

Naturally, the task of deformation-based bridge condition assessment goes beyond the acquisition of measurements on bridge deformation. However, deformation can be used as indicator of structural damage for certain damage types. By simulating the expected deformation in different structural conditions, thereby specifically accounting for temperature-based deformation, and comparing the modelled deformation with measurement results obtained through various remote sensing technologies, an assessment of the structural condition can be attempted. While the goal of this investigation was to provide a contrasting juxtaposition of measurement techniques, thereby focusing on the acquisition of bridge shape data and consequent evaluation of bridge deformation, some of the acquired data can also be used for further processing to identify the actual condition of the bridge and thus provide help in bridge assessment and maintenance planning.

Acknowledgements The authors would like to acknowledge the Austrian Research Promotion Agency FFG for financial support through the project VerBewIng (FFG 871524: 'Deformation-based Assessment of Engineering Structures'). Visualisations were created using ggplot2 (Wickham 2016) and QGIS 3.24 (QGIS Association 2022).

Author Contributions MS: conceptionalisation of the study, draft manuscript creation, InSAR analysis, visualisation; PD: UAV-ALS analysis; MK: thermal deformation modelling, FE modelling; MR: MLS analysis; RS: MLS analysis. All authors were jointly involved in discussing the results as well as writing the manuscript.

Data and Code Availability Sentinel-1 data are freely accessible online, e.g. through the Copernicus Open Access Hub (https://scihub.copernicus.eu/) or via the Alaska Satellite Facility (https://asf.alaska.edu/). A supplementary animation showing vertical bridge deformation of Seitenhafenbrücke (Vienna, Austria) based on Sentinel-1 InSAR (PSI) and in-situ measurements is available on Figshare at https://doi.org/10.6084/m9.figshare.20035364.

Declarations

Conflict of interest The authors declare that they have no conflict of interest.

References

Alemdar ZF, Browning J, Olafsen J (2011) Photogrammetric measurements of RC bridge column deformations. Eng Struct 33(8):2407–2415. https://doi.org/10.1016/j.engstruct.2011.04.015

Arastounia M (2016) Automated as-built model generation of subway tunnels from mobile LiDAR data. Sensors 16(9):1486. https://doi.org/10.3390/s16091486

Arsoy S (2008) Proposed mathematical model for daily and seasonal thermal bridge displacements. Transp Res Rec J Transp Res Board 2050(1):3–12. https://doi.org/10.3141/2050-01

Bao Y, Chen Z, Wei S, Xu Y, Tang Z, Li H (2019) The state of the art of data science and engineering in structural health monitoring. Engineering 5(2):234–242. https://doi.org/10.1016/j.eng.2018.11.027

Bekaert D, Walters R, Wright T, Hooper A, Parker D (2015) Statistical comparison of InSAR tropospheric correction techniques. Remote Sens Environ 170:40–47. https://doi.org/10.1016/j.rse.2015.08.035

Besl P, McKay ND (1992) A method for registration of 3-D shapes. IEEE Trans Pattern Anal Mach Intell 14(2):239–256. https://doi.org/10.1109/34.121791

BEV (2022) APOS-Austrian Positioning Service. https://www.bev.gv.at/portal/page?_pageid=713,3175360&_dad=portal&_schema=PORTAL

Casas JR, Cruz PJS (2003) Fiber optic sensors for bridge monitoring. J Bridge Eng 8(6):362–373. https://doi.org/10.1061/(asce)1084-0702(2003)8:6(362)

Cleveland RB, Cleveland WS, McRae JE, Terpenning I (1990) STL: a seasonal-trend decomposition procedure based on LOESS. J Off Stat 6(1):3–73

Cleveland WS, Grosse E, Shyu WM (2017) Local regression models. In: Statistical Models in S, pp 309–376. Routledge. https://doi.org/10.1201/9780203738535-8

Crosetto M, Solari L, Mróz M, Balasis-Levinsen J, Casagli N, Frei M, Oyen A, Moldestad DA, Bateson L, Guerrieri L, Comerci V, Andersen HS (2020) The evolution of wide-area DInSAR: from regional and national services to the European Ground Motion Service. Remote Sens 12(12):2043. https://doi.org/10.3390/rs12122043

Delgado Blasco J, Foumelis M, Stewart C, Hooper A (2019) Measuring urban subsidence in the Rome metropolitan area (Italy) with Sentinel-1 SNAP-StaMPS persistent scatterer interferometry. Remote Sens 11(2):129. https://doi.org/10.3390/rs11020129

Delgado Blasco JM, Foumelis M (2018) Automated SNAP Sentinel-1 DInSAR processing for StaMPS PSI with open source tools. 10.5281/ZENODO.1308835

EPOSA (2022) Echtzeit positionierung austria. https://www.eposa.at

ESA (2021) Sentinel-1 SAR Technical Guide: Level-1 Interferometric Wide Swath SLC Products. https://sentinels.copernicus.eu/web/sentinel/technical-guides/sentinel-1-sar/products-algorithms/level-1/single-look-complex/interferometric-wide-swath

ESA/ATG medialab (2014) Sentinel-1 radar vision. https://www.esa.int/ESA_Multimedia/Images/2014/01/Sentinel-1_radar_vision

Foumelis M, Blasco JMD, Desnos YL, Engdahl M, Fernandez D, Veci L, Lu J, Wong C (2018) ESA SNAP-StaMPS integrated processing for Sentinel-1 persistent scatterer interferometry. In: IGARSS 2018-2018 IEEE International Geoscience and Remote Sensing Symposium. IEEE. https://doi.org/10.1109/igarss.2018.8519545

Friedman JH (1984) A variable span smoother. Laboratory for Computational Statistics, Stanford University, Tech Rep Technical Report No.5

Geier R, Mack T, Krebes E (2014) Monitoring der seitenhafenbrücke in wien. Beton Stahlbetonbau 109(7):486–495. https://doi.org/10.1002/best.201400023

Genolini C, Alacoque X, Sentenac M, Arnaud C (2015) kmlandkml3d:RPackages to cluster longitudinal data. J Stat Softw. https://doi.org/10.18637/jss.v065.i04

Hooper A, Bekaert D, Spaans K, Arıkan M (2012) Recent advances in SAR interferometry time series analysis for measuring crustal deformation. Tectonophysics 514–517:1–13. https://doi.org/10.1016/j.tecto.2011.10.013

Hyndman RJ, Khandakar Y (2008) Automatic time series forecasting: the forecast package for R. J Stat Softw. https://doi.org/10.18637/jss.v027.i03

Kalenjuk S, Lienhart W, Rebhan M, Marte R (2019) Large-scale monitoring of retaining structures: new approaches on the safety assessment of retaining structures using mobile mapping. In: Wang KW, Sohn H, Huang H, Lynch JP (eds) Sensors and smart structures technologies. SPIE. https://doi.org/10.1117/12.2513856

Kral H, Kuhnle T, Spindlböck S, Kolik G (2012) Die seitenhafenbrücke in wien. Beton Stahlbetonbau 107(3):183–191. https://doi.org/10.1002/best.201100087

Lazecky M, Hlavacova I, Bakon M, Sousa JJ, Perissin D, Patricio G (2017) Bridge displacements monitoring using space-borne X-band SAR interferometry. IEEE J Sel Top Appl Earth Obs Remote Sens 10(1):205–210. https://doi.org/10.1109/jstars.2016.2587778

Li Z, Hou G, Wang K, Hu J (2021) Deformation monitoring of cracked concrete structures based on distributed optical fiber sensing technology. Opt Fiber Technol 61(102):446. https://doi.org/10.1016/j.yofte.2020.102446

Macchiarulo V, Milillo P, Blenkinsopp C, Giardina G (2022) Monitoring deformations of infrastructure networks: a fully automated GIS integration and analysis of InSAR time-series. Struct Health Monit. https://doi.org/10.1177/14759217211045912

McElhinney CP, Kumar P, Cahalane C, McCarthy T (2010) Initial results from European road safety inspection (eursi) mobile mapping project. In: International archives of photogrammetry, remote sensing and spatial information sciences, vol XXXVIII. International society of photogrammetry and remote sensing (ISPRS), Newcastle upon Tyne, pp 440–445

Middleton CR, Fidler PR, Vardanega PJ (2016) Bridge monitoring: a practical guide. ICE Publishing, London

Moorty S, Roeder CW (1992) Temperature-dependent bridge movements. J Struct Eng 118(4):1090–1105. https://doi.org/10.1061/(asce)0733-9445(1992)118:4(1090)

Mukupa W, Roberts GW, Hancock CM, Al-Manasir K (2016) A review of the use of terrestrial laser scanning application for change detection and deformation monitoring of structures. Surv Rev. https://doi.org/10.1080/00396265.2015.1133039

Nothegger C (2011) Improving completeness of geometric models from terrestrial laser scanning data. In: Proceedings of the 23rd CIPA Symposium, CIPA, Prague, Czech Republic

Praxmarer L, Reiterer M (2007) Bauwerkserhaltung am beispiel der murbrücke st. lorenzen. In: Brückentagung, Österreichische Vereinigung für Beton und Bautechnik, Wien

Puente I, González-Jorge H, Martínez-Sánchez J, Arias P (2013) Review of mobile mapping and surveying technologies. Measurement 46(7):2127–2145. https://doi.org/10.1016/j.measurement.2013.03.006

QGIS Association (2022) QGIS Geographic Information System. http://www.qgis.org

Qin X, Li Q, Ding X, Xie L, Wang C, Liao M, Zhang L, Zhang B, Xiong S (2021) A structure knowledge-synthetic aperture radar interferometry integration method for high-precision deformation monitoring and risk identification of sea-crossing bridges. Int J Appl Earth Obs Geoinf 103(102):476. https://doi.org/10.1016/j.jag.2021.102476

Rashidi M, Mohammadi M, Kivi SS, Abdolvand MM, Truong-Hong L, Samali B (2020) A decade of modern bridge monitoring using terrestrial laser scanning: review and future directions. Remote Sens 12(22):3796. https://doi.org/10.3390/rs12223796

Roeder CW (2003) Proposed design method for thermal bridge movements. J Bridge Eng 8(1):12–19. https://doi.org/10.1061/(asce)1084-0702(2003)8:1(12)

Sanio D, Mark P, Ahrens MA (2017) Temperaturfeldberechnung für brücken. Beton Stahlbetonbau 112(2):85–95. https://doi.org/10.1002/best.201600068

Schlögl M, Widhalm B, Avian M (2021) Comprehensive time-series analysis of bridge deformation using differential satellite radar interferometry based on Sentinel-1. ISPRS J Photogramm Remote Sens 172:132–146. https://doi.org/10.1016/j.isprsjprs.2020.12.001

Schlögl M, Gutjahr K, Fuchs S (2022) The challenge to use multitemporal InSAR for landslide early warning. Nat Hazards. https://doi.org/10.1007/s11069-022-05289-9

Selvakumaran S, Webb G, Bennetts J, Middleton C, Rossi C (2019) Waterloo bridge monitoring: comparing measurements from earth and space. In: International conference on smart infrastructure and construction 2019 (ICSIC). ICE Publishing. https://doi.org/10.1680/icsic.64669.639

Seo J, Hu JW, Lee J (2016) Summary review of structural health monitoring applications for highway bridges. J Perform Constr Facil 30(4):04015072. https://doi.org/10.1061/(asce)cf.1943-5509.0000824

Wang X, Zhao Q, Xi R, Li C, Li G, Li L (2021) Review of bridge structural health monitoring based on GNSS: from displacement monitoring to dynamic characteristic identification. IEEE Access 9:80043–80065. https://doi.org/10.1109/access.2021.3083749

Wickham H (2016) ggplot2: elegant graphics for data analysis. Springer, New York

Wright MN, Ziegler A (2017) Ranger: a fast implementation of random forests for high dimensional data in C++ and R. J Stat Softw. https://doi.org/10.18637/jss.v077.i01

Xi R, Jiang W, Meng X, Chen H, Chen Q (2018) Bridge monitoring using BDS-RTK and GPS-RTK techniques. Measurement 120:128–139. https://doi.org/10.1016/j.measurement.2018.02.001

Ye C, Acikgoz S, Pendrigh S, Riley E, DeJong M (2018) Mapping deformations and inferring movements of masonry arch bridges

using point cloud data. Eng Struct 173:530–545. https://doi.org/10.1016/j.engstruct.2018.06.094

Yu C, Li Z, Penna NT, Crippa P (2018) Generic atmospheric correction model for interferometric synthetic aperture radar observations. J Geophys Res Solid Earth 123(10):9202–9222. https://doi.org/10.1029/2017jb015305

Zan FD, Guarnieri AM (2006) TOPSAR: Terrain observation by progressive scans. IEEE Trans Geosci Remote Sens 44(9):2352–2360. https://doi.org/10.1109/tgrs.2006.873853

Zhou Y, Xia Y, Chen B, Fujino Y (2020) Analytical solution to temperature-induced deformation of suspension bridges. Mech Syst Signal Process 139(106):568. https://doi.org/10.1016/j.ymssp.2019.106568

Zhou Y, Xia Y, Fujino Y (2021) Analytical formulas of beam deflection due to vertical temperature difference. Eng Struct 240(112):366. https://doi.org/10.1016/j.engstruct.2021.112366